ACS APPLIED MATERIALS & INTERFACES

Research Article

www.acsami.org

Enhanced Energy Storage Density in Poly(Vinylidene Fluoride) Nanocomposites by a Small Loading of Suface-Hydroxylated $Ba_{0.6}Sr_{0.4}TiO_3$ Nanofibers

Liu Shaohui, Zhai Jiwei,* Wang Jinwen, Xue Shuangxi, and Zhang Wenqin

Functional Materials Research Laboratory, Tongji University, Shanghai 200092, China

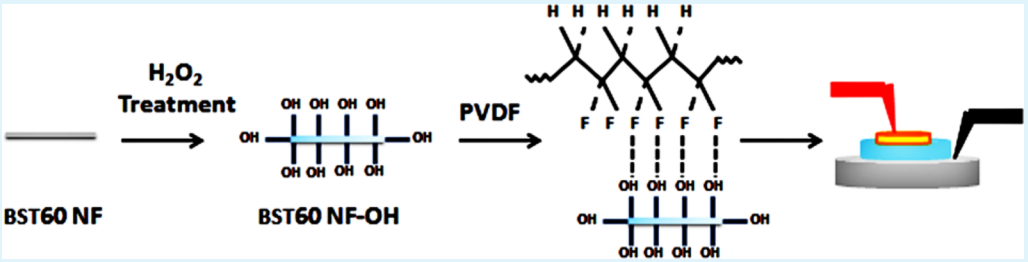

ABSTRACT: The ceramic−polymer nanocomposites consisting of $Ba_{0.6}Sr_{0.4}TiO_3$ nanofibers (BST60 NF) with a large aspect ratio prepared via electrospinning and employing surface hydroxylated as fillers and poly(vinylidene fluoride) (PVDF) as matrix have been fabricated by a solution casting method. The nanocomposites exhibit enhanced permittivity, reduced loss tangents and improved breakdown electric field strength at a low volume fraction of hydroxylated BST60 NF. The energy density of the nanocomposites is significantly enhanced, and the maximal energy density of 6.4 J/cm^3 is obtained in the composite material with 2.5 wt % hydroxylated BST60 NF, which is more than doubled as compared with the pure PVDF. Such significant enhancements result from combined effect of the large aspect ratio, the surface modification and the improved crystallinity of the nanocomposites induced by the hydroxylated BST60 NF. This work may provide a route for using the hydroxylated ceramic nanofibers to enhance the dielectric energy density in ceramic−polymer nanocomposites.

KEYWORDS: *$Ba_{0.6}Sr_{0.4}TiO_3$ nanofiber, energy density, nanocomposites, surface hydroxylation*

INTRODUCTION

High energy density capacitors are currently gaining worldwide interest because of their great potential applications in the fields of advanced electronic devices and electric power systems.[1−6] Generally, The quality of the stored energy density, U, of the linear dielectric materials is equal to $U = (1/2)\varepsilon_0\varepsilon_{eff}E_b$ (where ε_0, ε_{eff} and E_b are the vacuum permittivity, the relative permittivity and the breakdown strength, respectively), and the stored energy, U, in dielectric materials is calculated from the polarization−electric field hystersis (D−E) loops, by the formula $U = \int EdD$ (E is applied electric field, D is electric displacement). On the basis of these equations, it is indicated that the value of energy storage density could be improved by increasing the critical breakdown strength and enhancing permittivity (polarization). However, it is very difficult to optimize them synchronously. To date, dielectric polymers, such as poly(vinylidene fluoride) (PVDF), are flexible and easy to process and have a high breakdown strength but are limited by their low intrinsic permittivity.[7] Whereas ferroelectric ceramics, such as $Pb(Zr,Ti)O_3$, $Ba_{1-x}Sr_xTiO_3$ and $BaTiO_3$, have a high permittivity but are brittle and have a low breakdown strength.[8] As a result, there has been much effort to prepare polymer nanocomposites through the incorporation of surface modification of the nanoparticles with high permittivity fillers dispersed in a matrix, with the hope of preparing nanocomposites containing the high permittivity of the ceramic fillers and the high breakdown strength of polymers.[9] However, the breakdown strength of nanocomposites sharply decreases at a high volume fraction of fillers. To maintain a high breakdown strength and consequently a high energy storage density capacitor, the nanocomposites are prepared at a low volume fraction of filler.[10]

Compared to the $Ba_{0.6}Sr_{0.4}TiO_3$ (BST60) nanoparticles, the BST60 nanofibers (BST60 NF)[11,12] with large aspect ratios are more effective in enhancing the permittivity of nanocomposites at low concentrations, which provide a route for using the ceramic nanofibers to enhance the dielectric energy storage density in polymer nanocomposites. Song[13] showed that the increase of ε_{eff} and E_b at a small loading of BST60 NF can afford significantly enhanced extractable energy storage densities in the PVDF matrix nanocomposites. The BST60 NF are able to increase the permittivity of the nanocomposites at much lower concentration due to their large dipole moments, and their smaller specific surface can help to reduce the surface energy and thus prevent the nanofillers from agglomerating in the polymer matrix. At the same time, the

Received: September 26, 2013
Accepted: January 10, 2014
Published: January 10, 2014

interface between the fillers and the polymer matrix of the nanocomposites plays an important role in the energy storage nanocomposites.[14] The surface modification could facilitate the dispersion of the fillers in the polymer matrix and strongly chain with the polymer matrix by chemical bonds in the interfacial layer, which can improve the energy storage density of the nanocomposites.[15]

The shape of the fillers and the interface between the fillers and the polymer matrix are the important factors determining the energy storage density of the ceramic nanoparticle based polymer nanocomposites. There are few reports on the preparation of BST60 NF by employing surface hydroxylated as fillers in PVDF-based nanocomposites. In this study, we report the successful fabrication of BST60 NF with a large aspect ratio via electrospinning and surface hydroxylation as dielectric fillers in PVDF-based nanocomposites. The BST60 NFs with high permittivity and large aspect ratios give rise to the increased permittivity and dielectric breakdown strength of the nanocomposite at a small loading, which afford significantly enhanced energy storage densities in the nanocomposites.

EXPERIMENTAL SECTION

The BST60 NF prepared via electrospinning are employed as dielectric fillers in PVDF-based nanocomposites. The 0.726 g Barium acetate (99.0%, Alfa Aesar) and 0.411 g Strontium acetate hemihydrate (99.0%, Alfa Aesar) was dissolved in 5 mL acetic acid and stirred for 1 h. Meanwhile, the 1.612 g of Titanium(IV) *n*-butoxide (99.0%, Alfa Aesar) was dissolved in 5 mL of acetylacetone and stirred for 1 h. Then the dissolved solution of all compounds were mixed with a solution consisting of poly(vinyl pyrrolidone) (PVP, MW = 1 300 000) dissolved in ethanol (PVP: 2 g and ethanol: 3 mL). The mixture was stirred at room temperature for 1 h to achieve complete dissolution and mixing. Ultimately, a lucid and viscous sol solution was obtained for electrospinning. The precursor sol solution was loaded into a 10 mL plastic syringe with a syringe needle of which the internal diameter was 0.5 mm. The needle was connected to a DC high-voltage power supply. In our experiment, a voltage of 15 kV was applied between the cooper plate collector and the syringe needle with a distance of 12 cm. The composite nanofibers were collected on the plate during electrospinning processes and annealed at 650 °C for 3 h in air to remove PVP.

The BST60 NF were dispersed in an aqueous solution of H_2O_2 (35%, 350 mL) and heated to 100 °C for 3 h, and then centrifuged the solution. The nanocomposites were prepared by dispersing the surface hydroxylated BST60 NF (BST60 NF−OH) into a PVDF (3F Co., China.)/*N*,*N*-dimethylformamide (DMF) solution under vigorous stirring at 40 °C for 2 h. The solution was cast onto an Indium Tin Oxide (ITO) glass and dried under vacuum at 60 °C for 10 h. The obtained films were heated at 200 °C for 10 min and quenched in an ice−water bath immediately. The composite films were about 10 μm in thickness.

CHARACTERIZATION

X-ray diffraction (XRD) (D8 Advanced, Bruker, Germany) was employed to investigate the crystal structure of nanofibers using Cu Kα radiation. Microstructural observations of samples were analyzed using scanning electron microscopy (SEM) (XL30-FEG, Philips, The Netherlands). Thermogravimetric analysis (TGA) and differential scanning calorimetry (DSC) were conducted using a NETZSCH STA449C instrument under nitrogen atmosphere at the heating rate of 10 °C/min. Dielectric properties were measured using a E4980A LCR meter (Agilent, Palo Alto, CA, USA) in the frequency range of 100 Hz to 2 MHz. The breakdown strength (BDS) was tested by Dielectric Withstand Voltage Test (ENTAI, Nanjing, China). BDS measurements were measured in a silicone oil bath at room temperature (25 °C) by applying a DC voltage ramp with a rate of rise of 200 V s^{-1} and a limit current of 5 mA. A set of 10 samples was employed for each condition. The nanocomposite films are square shape 1 × 1 cm^2 and about 10 μm in thickness. The top gold electrodes with 2 mm in diameter and a thickness of 40 nm were sputtered on surfaces of the nanocomposites films using a shadow mask. And bottom electrode sputtered on surfaces of the nanocomposites films. Samples were inserted between two stainless steel columnar electrodes (Φ = 1 mm). The polarization−electric field loops (P−E) were measured by a Premier II ferroelectric test system in a silicone oil bath to avoid electrical discharges that would occur in air. The top gold electrodes with 2 mm in diameter and a thickness of 40 nm were sputtered on surfaces of the nanocomposites films using a shadow mask. The bottom electrode was the ITO glass.

RESULTS AND DISCUSSION

Figure 1a,b exhibits the SEM images of BST60/PVP composite nanofibers before and after calcinations, respectively. It can be seen that the surfaces of the composite fibers before calcination were smooth. They are several millimeters long with a diameter

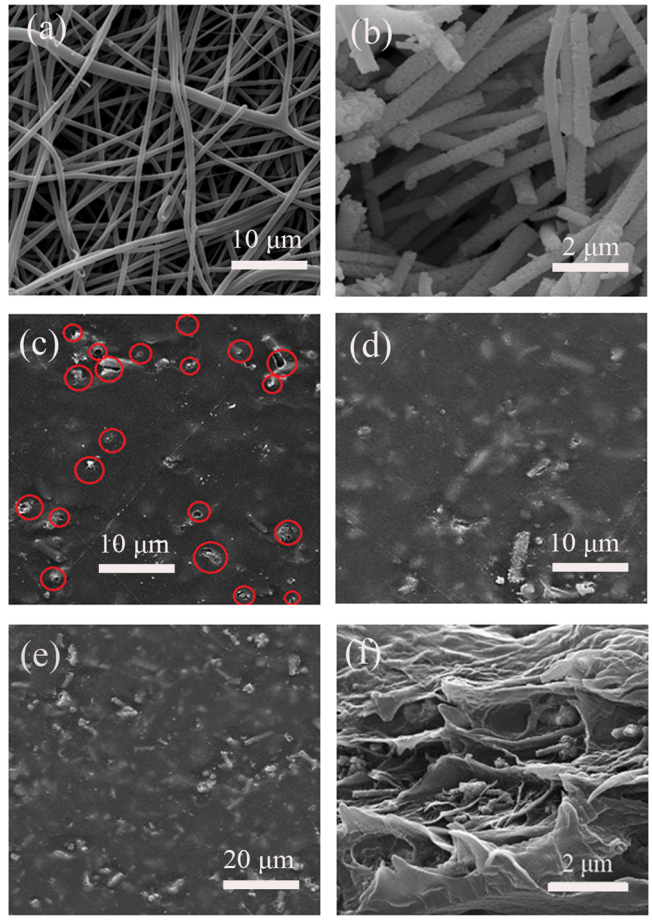

Figure 1. (a) BST60/PVP composite nanofibers before calcinations, (b) BST60 NF, (c) the surface SEM of 5 vol % BST60 NF/PVDF nanocomposites and (d) the 5 vol % BST60 NF−OH/PVDF nanocomposites, (e) the 10 vol % BST60 NF−OH/PVDF nanocomposites and (f) cross-section SEM of 5 vol % BST60 NF−OH/PVDF nanocomposites.

dx.doi.org/10.1021/am4042096 | ACS Appl. Mater. Interfaces 2014, 6, 1533−1540

of approximately 300 nm. After calcinations at 650 °C, the diameters of the nanofibers shrank drastically to 100−200 nm due to the decomposition of PVP and the transformation from metal salts into metal oxides, BST60 NF are 10 μm long as shown in Figure (b). Figure 1c,d shows the typical surface SEM images of 5 vol % BST60 NF/PVDF nanocomposites and the 5 vol % BST60 NF−OH/PVDF nanocomposites. Compared to the SEM images of BST60 NF/PVDF nanocomposites, the BST60 NF−OH/PVDF nanocomposites have hardly any small voids between the BST60 NF and PVDF. This result indicates the surface-hydroxylated BST nanofibers could not only facilitate its dispersion in the polymer matrix but also strongly chain with the polymer matrix by hydroxy bonds in the interface. Moreover, Figure 1d,f,e shows the surface SEM images of the 5 vol % BST60 NF−OH/PVDF nanocomposites, the 10 vol % BST60 NF−OH/PVDF nanocomposites and cross-section SEM of 5 vol % BST60 NF−OH/PVDF nanocomposites, suggesting that the nanofibers have been successfully transferred to the polymer matrix with minimum agglomeration from solution and BST60 NF−OH tend to orient in the in-plane directions of the composite films.

Figure 2 shows the XRD patterns of BST60 NF prepared via electrospinning and BST60 NF−OH. It can be seen that eight

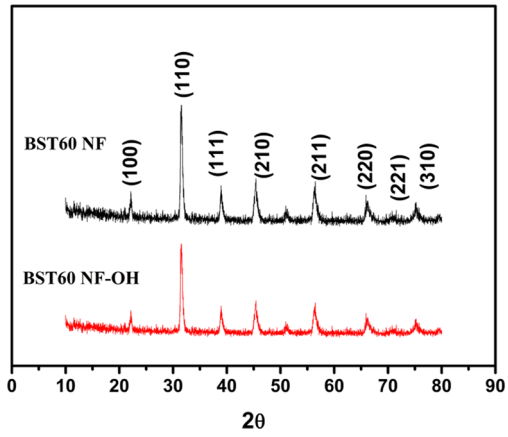

Figure 2. XRD patterns of BST60 NF and BST60 NF−OH.

diffraction patterns at θ = 22.399, 31.867, 39.312, 45.733, 51.486, 56.802, 66.640, 71.322 and 75.820 correspond to (100), (110), (111), (200), (210), (211), (220), (221) and (310) characteristic peaks of BST60 with cubic crystalline. And XRD results exhibit no changes in the sample of the crystal structure of both BST NF−OH and untreated BST NF.

TGA curves (Figure 3) present the evidence to confirm the evolution of surface hydroxylated BST60 NF. It can be seen from Figure 3 that (i) the weight loss of the nanofibers shows the sequence of BST60 NF < BST60 NF−OH at 1000 °C; (ii) BST60 NF−OH show the maximum weight loss before 300 °C, indirectly confirming that the hydroxylate groups were introduced onto the surface of BST60 NF−OH.[16]

FTIR is used to confirm the hydroxylation of the nanofibers. Figure 4 shows the FTIR spectra of the modified and unmodified BST60 NF−OH. The new band at 3447 cm^{-1} is associated to the stretcing mode of −OH, which comes from the hydroxylation of BST60 NF by the H_2O_2. The surface modification of the BST60 NF by the H_2O_2 is demonstrated to act as a bridge to between the F atoms on the PVDF and the −OH groups on the surface BST60 NF−OH (Figure 5).

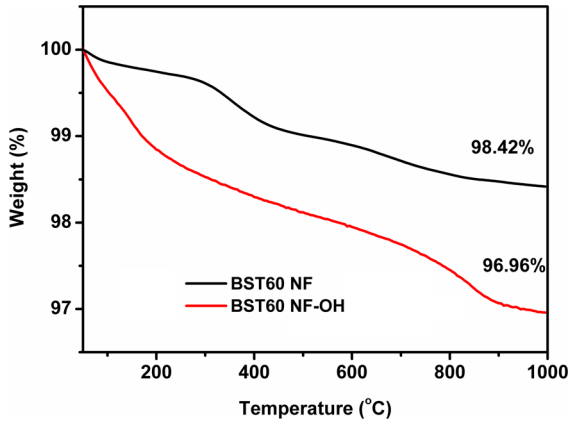

Figure 3. TGA curves for the BST60 NF and BST60 NF−OH.

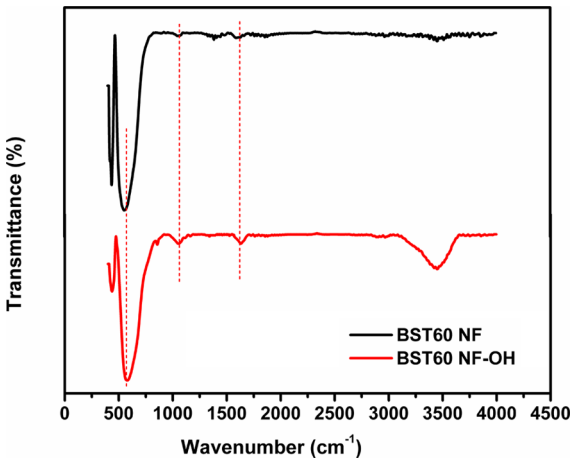

Figure 4. FTIR spectra of the BST60 NF and BST60 NF−OH.

To investigate the influences of the incorporation of the ceramic nanofibers in the polymer matrix, the DSC curves of the nanocomposites obtained during the cooling scan process are presented in Figure 6. The results illustrate that the nanofibers in the nanocomposites increase the crystallization temperature by 3 °C, from 133 °C in the pure polymer to 136 °C in the nanocomposite with 10 vol % BST60 NF−OH, which shows indeed the nanofibers facilitate the crystallization process in the polymer matrix. The degree of crystallinity was evaluated by $X_c = (H_f)/(H_f^0\omega)$, where H_f is the enthalpy of the melting transition of nanocomposite. H_f^0 = 104.7 J/g is the enthalpy of 100% crystalline PVDF. The crystallinity degree calculated from the samples is 20.2% for PVDF and 25.1%, 23.4%, 26.9%, 29.4% for PVDF nanocomposites with 2.5 vol %, 5.0 vol %,7.5 vol %, 10 vol % BST60 NF, respectively. The crystallinity degree calculated from the samples is 20.2% for PVDF and 29.9%, 27.4%, 31.9%, 34.4% for PVDF nanocomposites with 2.5 vol %, 5.0 vol %, 7.5 vol %, 10 vol % BST60 NF−OH, respectively. The BST 60 NF−OH acts as a nucleating agent and improves the degree of crystallinity of the PVDF, which indicates that the incorporation of BST 60 NF−OH has positive influences on increasing the crystallinity of the polymer matrix.[17]

Dependence of relative permittivity and loss tangent at 1 kHz of the BST60 NF/PVDF and BST60 NF−OH/PVDF nanocomposites are shown in Figure 7. As seen, the relative permittivity of the nanocomposites increases with the content of the BST60 NF−OH and reaches up to 25 at small loading of

dx.doi.org/10.1021/am4042096 | ACS Appl. Mater. Interfaces 2014, 6, 1533−1540

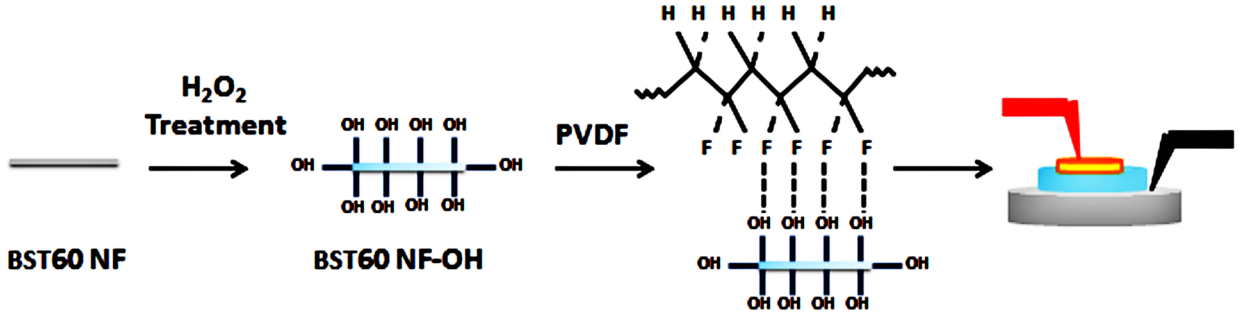

Figure 5. Schematic diagrams of the hydroxylation of BST60 NF and formation a bridge between the F atoms on the PVDF and the −OH groups on the surface of BST60 NF−OH.

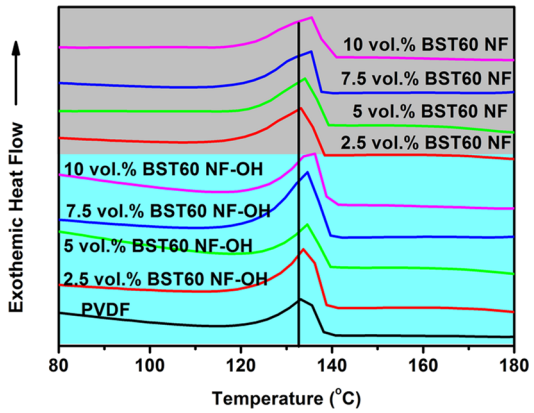

Figure 6. DSC curves obtained during the cooling cycle of the PVDF and the nanocomposites with various concentrations of BST60 NF and BST60 NF−OH.

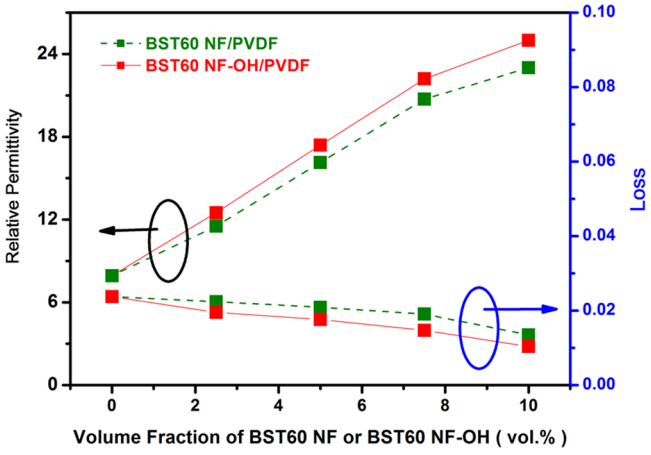

Figure 7. Relative permittivity and loss tangent of BST60 NF/PVDF and BST60 NF−OH/PVDF nanocomposites loaded with various concentrations of fillers measured at 1 kHz.

10 vol % BST60 NF−OH, which is mainly attributed to the higher relative permittivity and the large aspect ratio of BST60 NF−OH. The relative permittivity of both nanocomposites with the treated BST60 NF and those with untreated BST60 NF exhibits slight difference. And the relative permittivity of the BST60 NF−OH/PVDF is bigger than that of the BST60 NF/PVDF. The loss of the BST60 NF−OH/PVDF is lower than that of the BST60 NF/PVDF. This phenomenon can be explained as follows. Combining with the results of the SEM discussed above, the BST60 NF/PVDF have many defects such as voids in the nanocomposites, which means that the air was introduced in nanocomposites. Because the permittivity of air is low, the relative permittivity of BST60 NF/PVDF is decreased compared with BST60 NF−OH/PVDF nanocomposites.

Figure 8 shows the temperature dependence of the relative permittivity and loss tangent of the PVDF (Figure 8a), 10 vol % BST60 NF−OH/PVDF nanocomposite (Figure 8b) and 10 vol % BST60 NF/PVDF nanocomposite (Figure 8c) measured at the frequency of 10^3, 10^4, 10^5 and 10^6 Hz in the temperature range from −35 to +125 °C. It is obvious that over the whole measured temperature range, the addition of BST60 NF−OH results in an increase of the relative permittivity and a decrease of the loss. Another distinctive feature of the relative permittivity data is that the broad relative permittivity maximum and shift to higher temperatures with frequency, typical for relaxor ferroelectrics,[17] which corresponds to the dipolar freezing transition in which different frequency components of the polarization response will freeze at different temperature.[18] Furthermore, The temperature dependence of the relative permittivity of both nanocomposites with the treated BST60 NF and those with untreated BST60 NF exhibits slight difference. The loss of BST60 NF/PVDF is higher than that of the BST60 NF−OH/PVDF. The permittivity properties of the pure PVDF polymer and BST60 NF−OH/PVDF exhibits a sharp increase at 10^3 and 10^4 Hz and above 55 °C, where the space charge contribution (conduction) causes a large increase of both the relative permittivity and loss with temperature in the polymer. This phenomenon is allotted to an interfacial polarization, known as the Maxwell−Wagner−Sillars (MWS) effect. The origin of the MWS polarization in heterogeneous media exhibits the presence of the blocked charge carriers (impurities) in the polymeric phase arising from the manufacturing of the nanocomposites. The MWS polarization in the BST60 NF−OH/PVDF includes MWS_{PVDF} (these ions can then move toward the interfaces between the crystals and amorphous regions in PVDF) and $MWS_{BST60\ NF-OH/PVDF}$ (these ions can then move toward the interfaces between BST60 NF−OH fillers and polymer matrix in the BST60 NF−OH/PVDF). Because of the discrepancies of dielectric properties (conductivity, permittivity) of these two media, leading to the appearance of an interfacial polarization, which usually play an important role in determining the dielectric properties of composites.

To illustrate the interfacial polarization in the composites, the frequency dependence of the imaginary electric modulus (M″) of the PVDF and the composites at 100 °C is shown in Figure 9. The relaxation peak at about 735 Hz is attributed to MWS_{PVDF} relaxation, which is due to the charge accumulation on the boundary between the crystals and amorphous regions

dx.doi.org/10.1021/am4042096 | ACS Appl. Mater. Interfaces 2014, 6, 1533−1540

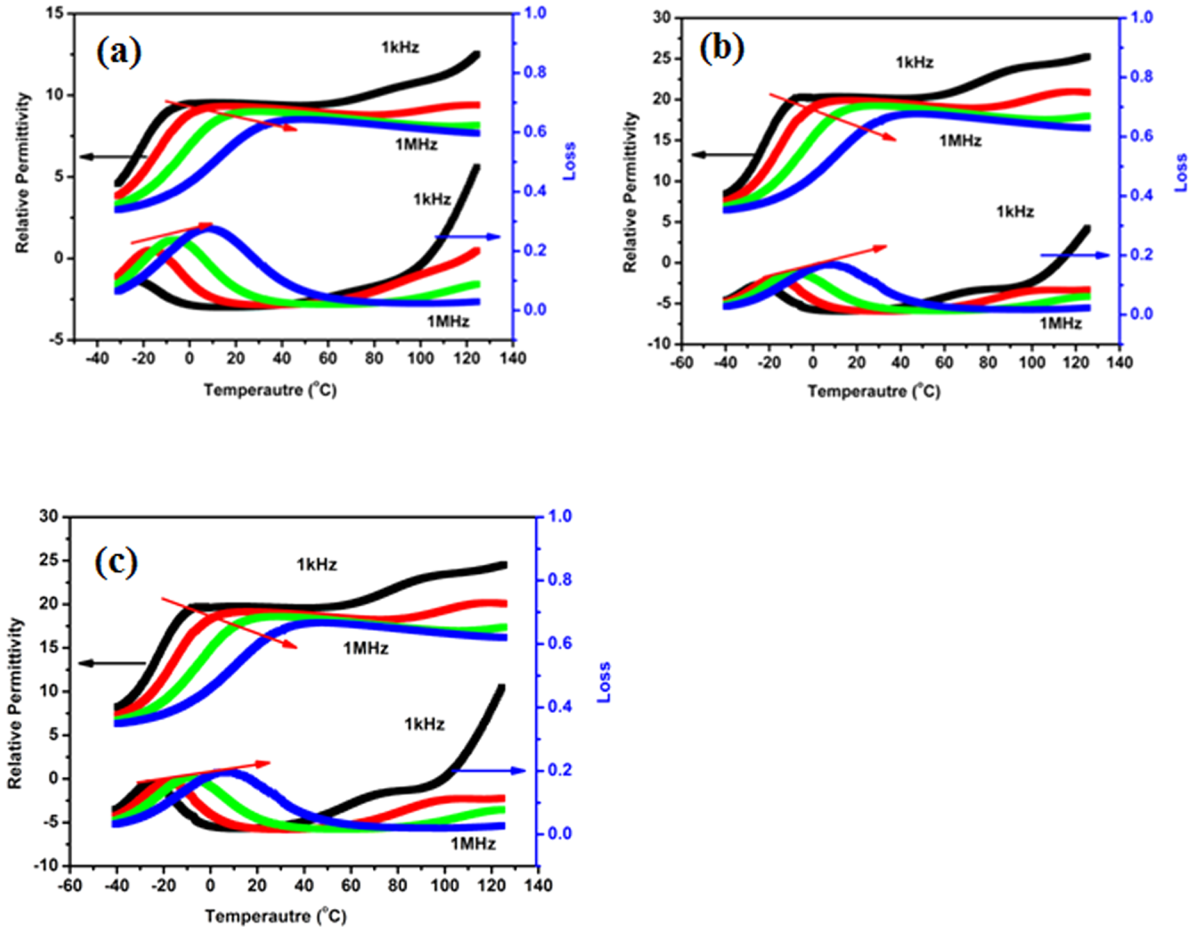

Figure 8. The temperature dependence of the permittivity and loss of the PVDF (a), 10 vol % BST60 NF−OH/PVDF nanocomposite (b) and 10 vol % BST60 NF/PVDF nanocomposite (c) measured in the temperature range from −30 to +125 °C.

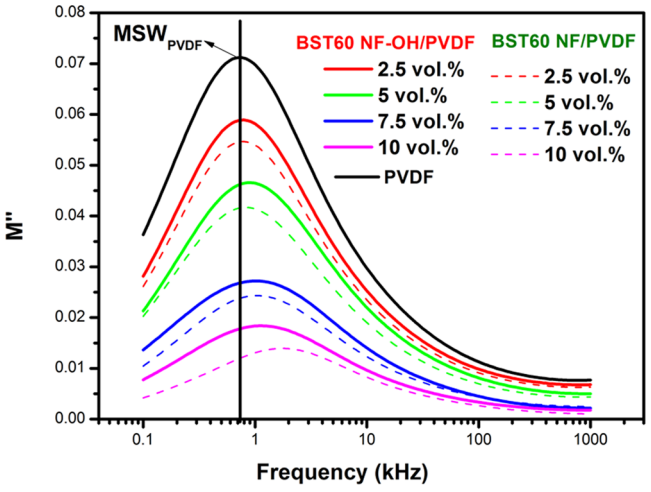

Figure 9. Frequency dependence of the M″ for nanocomposites with various concentrations of BST60 NF−OH and BST60 NF.

in PVDF. After introduction of the BST60 NF−OH, the relaxation intensity of MWS_{PVDF} polarization in the composites is much lower in comparison with the PVDF. But the peak of $MSW_{BST60\ NF-OH/PVDF}$ could not be observed due to the low BST60 NF−OH content. Another reason is that the MWS_{PVDF} polarization results in a suppressive effect on the $MWS_{BST60\ NF-OH/PVDF}$ polarization in the nanocomposites. The MWS_{PVDF} polarization relaxation peaks become broader with increasing BST60 NF−OH (or BST60 NF) loading. It is supposed that the $MWS_{BST60\ NF-OH/PVDF}$ polarization becomes more and more important with increases of the BST60 NF−OH content. After introduction of the BST60 NF−OH, the charge carriers also accumulate on the surface of BST60 NF−OH, which is the reason for the shift of the MWS_{PVDF} of BST60 NF−OH/PVDF nanocomposites to higher frequencies. All of these results are typical characteristics of MWS_{PVDF} polarization and are consistent with those observed in other polymer composites.[19−21] This is in agreement with the results of permittivity discussed above that the permittivity of the nanocomposites increases with the incorporation of NFs fillers.

The breakdown strength (BDS) is the key parameter in determining the energy storage density of nanocomposites. As a result of the improved BDS, the nanocomposites could be polarized under higher electric fields, giving rise to larger polarization. Figure 10 shows the BDS for BST60 NF/PVDF and BST60 NF−OH/PVDF nanocomposites loaded with various concentrations of fillers. Weibull plots of the electric strength for BST60/PVDF nanocomposites and BST60 NF−OH/PVDF nanocomposites loaded with various concentrations of fillers are shown in the inset. The Weibull distribution was utilized in this work to analyze the data of BDS. The mean BDS could be extracted from the data points where the fitting lines intersect with the horizontal line through $y = 0$. According to the fitting line, the BDS value of PVDF obtained from the x-intercept of the fitting line is 3670 kV/cm. With increases of the fillers concentration, the BDS value of the nanocomposites with

dx.doi.org/10.1021/am4042096 | ACS Appl. Mater. Interfaces 2014, 6, 1533−1540

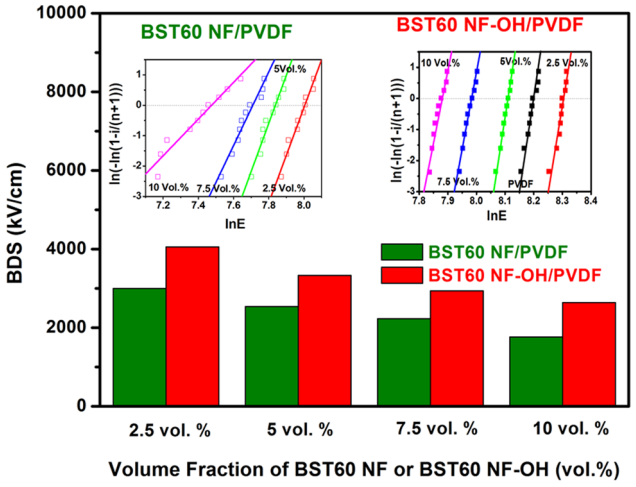

Figure 10. BDS for BST60 NF/PVDF and BST60 NF−OH/PVDF nanocomposites loaded with various concentrations of fillers. Weibull plots of the electric strength for BST60/PVDF and BST60 NF−OH/PVDF nanocomposites loaded with various concentrations of fillers are shown in the insets.

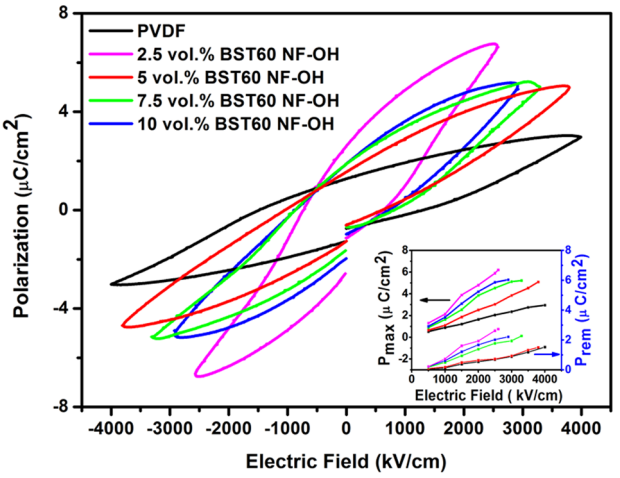

Figure 11. P−E curves of BST60 NF−OH/PVDF nanocomposites. The maximum polarization and remnant polarization of BST60 NF−OH/PVDF nanocomposites loaded with various concentrations fillers are shown in the inset.

2.5 vol % BST60 NF−OH rises to a maximum of 3980 kV/cm and then gradually decreases to a minimum of 2600 kV/cm with further addition of the BST60 NF−OH. The improvement of the BDS with a low concentration of nanofiber fillers has two reasons. First, the fillers by the surface modification could facilitate the dispersion of the BST60 NF in the polymer matrix and strongly chain with the polymer matrix by chemical bonds in the interface, which reduces the percolative pathways for the charge transfer and the mobility of the polymer chains.[22] Second, the surface modified BST60 NFs with large aspect ratio tend to orient in the in-plane directions of the composite films during the solution cast process. When the electric field applied in the out-of-plane direction of the composite films, the susceptibility of the nanocomposites could be reduced by the BST60 NF−OH perpendicular to the external electric field, leading to a lower concentration of electric field in the polymer matrix.[23] Compared to the results, it should be noted that the BST60 NF−OH/PVDF nanocomposites show higher BSD than that of the BST60 NF/PVDF nanocomposites at the same filler concentration. Combined with the results of the SEM discussed above, it might be due to the improved compatibility between the BST60 NF−OH and PVDF, which can decrease the defects such as voids in the nanocomposites and, in turn, can improve the BSD.

For the ferroelectrics, because the polarization is not linearly dependent on the electric field, the energy storage density should be calculated from the P−E loops. The P−E loops for PVDF-based nanocomposites with different amount of BST60 NF−OH are measured at frequency of 100 Hz. P−E curves of BST60 NF−OH/PVDF nanocomposites are shown in Figure 11. The maximum polarization and remnant polarization of BST60 NF−OH/PVDF nanocomposites loaded with various concentrations fillers are shown in the inset. Under the electric field of 2600 kV/cm, the saturated polarization of nancomposites increases consistently with increases in the volume fraction of BST60 NF−OH, and reaches a maximum value of 6.3 μC/cm^2 for nanocomposites of 10 vol % BST60 NF−OH. It is attributed that the permittivity of BST60 NF is larger than that of PVDF. Moreover, the interface areas in the nanocomposites would lead to the MWS interfacial polarization, which result from an "interaction zone" with the Gouy−Chapman diffuse layer and significantly enhances the polarization of the nanocomposites.[24] However, the continuous increase in the remnant polarization is also observed with increases of BST60 NF−OH. The high remnant polarization will decrease the discharge efficiency of capacitor because the charge cannot be fully discharged. At the same time, as the concentration of the filler increases, the BDS of the nanocomposites decreases sharply, which makes it difficult to obtain the polarization value of the nanocomposites under high electric field.

The extractable energy storage density is then derived from these D−E curves according to the formula $U = \int EdD$. The energy storage density of BST60 NF−OH/PVDF nanocomposites loaded with various concentrations of BST60 NF−OH as function of electric field calculated from D−E loops is shown in Figure 10. The maximal energy storage density of 6.4 J/cm^3 was obtained in the nanocomposites with 2.5 vol % BST60 NF−OH, which is more than doubled as compared with the pure PVDF. This value is increased significantly and exceeds those reported for the conventional polymer−ceramic composite.[25]

For the application of dielectric capacitors in practice, both a high energy density and a high efficiency (η) are desired. Figure 12 gives the energy density and efficiency (discharge energy/charge energy) of the nanocomposites with different BST60 NF−OH concentrations with increases of the electric field. It is clearly shown that the efficiency decreases with the applied electric filed, which is highly related to the conduction loss. As the concentration of the filler increases, the efficiency of the capacitor decreases due to the larger hysteresis in the polarization. However, at fields below 1000 kV/cm, the efficiency of the nanocomposites with 2.5 vol % BST60 NF−OH is bigger than 80% and still higher than 50% at an electric field of 3800 kV/cm.

Figure.13 gives the P−E loops of the nanocomposite of 2.5 vol % BST60 NF and that of 2.5 vol % BST60 NF−OH under various applied electric field. The 2.5 vol % BST60 NF−OH/PVDF nanocomposites exhibit narrow P−E loops, higher maximum polarization and much lower remnant polarization in comparison with the 2.5 vol % BST60 NF/PVDF.

dx.doi.org/10.1021/am4042096 | ACS Appl. Mater. Interfaces 2014, 6, 1533−1540

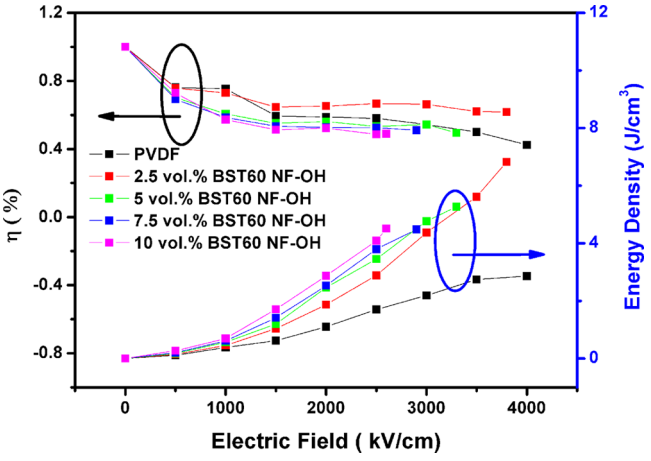

Figure 12. The efficiency and energy storage density of BST60 NF−OH/PVDF nanocomposites loaded with various concentrations fillers.

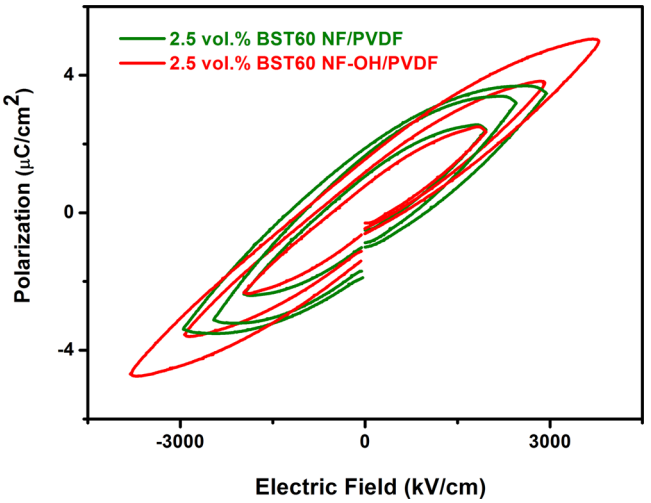

Figure 13. The P−E loops under various applied electric field for 2.5 vol % BST60 NF/PVDF and 2.5 vol % BST60 NF−OH/PVDF nanocomposites.

Figure 14 gives the discharged energy density and energy efficiency for 2.5 vol % BST60 NF/PVDF and 2.5 vol % BST60 NF−OH/PVDF under various applied electric fields. It can be seen that, compared with BST60 NF/PVDF, BST60 NF−OH/PVDF nanocomposites exhibit much higher energy efficiencies. More importantly, the 2.5 vol % BST60 NF−OH/PVDF nanocomposites show much higher discharged energy densities at high electric field values in comparison with the 2.5 vol % BST60 NF−OH/PVDF. These results clearly show the high effectiveness of surface hydroxylation on the enhancement of energy density of BST60 NF/PVDF.

CONCLUSIONS

In conclusion, the enhanced relative permittivity, reduced loss tangents and improved BDS were obtained in PVDF-based nanocomposites filled with surface modified BST60 NF. Moreover, the energy storage density of 6.4 J/cm^3 was obtained in the composite film with 2.5 wt % BST60 NF−OH, which is more than double the energy storage density of the pure PVDF. Such significant enhancement results from the combined effect of the large aspect ratio, the surface hydroxylation BST60 NF and the improved crystallinity of the polymer induced by the

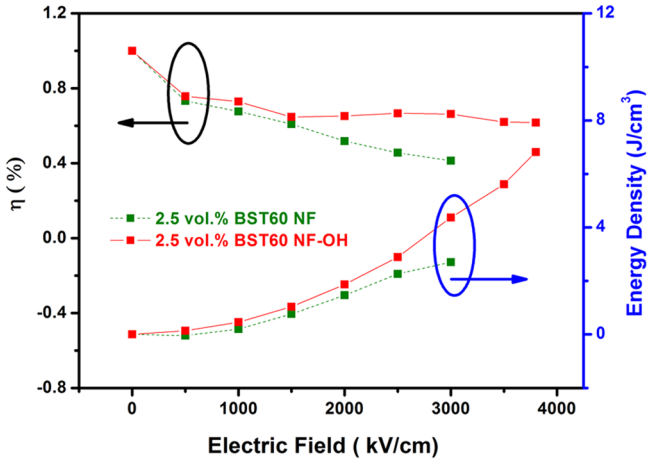

Figure 14. Energy density and energy efficiency under various applied electric field for 2.5 vol % BST60 NF/PVDF and 2.5 vol % BST60 NF−OH/PVDF nanocomposites.

BST60 NF−OH. The results suggest that the BST60 NF, by employing surface hydroxylated with the high aspect ratio, can be used to improve the energy storage density of nanocomposites, thus providing a route for using the ceramic nanofibers to enhance the dielectric energy storage density in polymer nanocomposites.

AUTHOR INFORMATION

Corresponding Author

*Z. Jiwei. Tel.: +86 21 65980544. Fax: +86 21 65985179. E-mail address: apzhai@tongji.edu.cn.

Notes

The authors declare no competing financial interest.

ACKNOWLEDGMENTS

This research was supported by the Ministry of Sciences and Technology of China through 973-project under Grant (2009CB623302) and the National 863 Program (2012AA03A706).

REFERENCES

(1) Barber, P.; Balasubramanian, S.; Anguchamy, Y.; Gong, S.; Wibowo, A.; Gao, H.; Ploehn, H. J.; Zur Loye, H.-C. *Materials* **2009**, *2*, 1697−1733.
(2) Tang, H. X.; Sodano, H. A. *Nano Lett.* **2013**, *13*, 1373−1379.
(3) Hu, P.; Song, Y.; Liu, H.; Shen, Y.; Lin, Y.; Nan, C.-W. *J. Mater. Chem. A* **2013**, *1*, 1688−1693.
(4) Avila, H. A.; Ramajo, L. A.; Goes, M. S.; Reboredo, M. M.; Castro, M. S.; Parra, R. *ACS Appl. Mater. Interfaces* **2013**, *5*, 505−510.
(5) Tang, H.; Lin, Y.; Sodano, H. A. *Adv. Energy Mater.* **2013**, *3*, 451−456.
(6) Xie, L. Y.; Huang, X. Y.; Huang, Y. H.; Yang, K.; Jiang, P. K. *ACS Appl. Mater. Interfaces* **2013**, *5*, 1747−1756.
(7) Han, R. X.; Jin, J. Z.; Khanchaitit, P.; Wang, J. K.; Wang, Q. *Polymer* **2012**, *53*, 1277−1281.
(8) Wang, Q.; Zhu, L. J. *J. Polym. Sci. Part B: Polym. Phys.* **2011**, *49*, 1421.
(9) Chu, B. J.; Zhou, X.; Ren, K. L.; Neese, B.; Lin, M. R.; Wang, Q.; Bauer, F.; Zhang, Q. M. *Science* **2006**, *313*, 334−336.
(10) Kim, P.; Doss, N. M.; Tillotson, J. P.; Hotchkiss, P. J.; Pan, M. J.; Marder, S. R.; Li, J. Y.; Calame, J. P.; Perry, J. W. *Acs Nano* **2009**, *3*, 2581−2492.
(11) Li, H. P.; Wu, H.; Lin, D. D.; Pan, W. *J. Am. Ceram. Soc.* **2009**, *92*, 2162−2164.

(12) Lee, D. Y.; Lee, K. H.; Lee, M. H.; Cho, N. I.; Kim, B. Y. *J. Sol–Gel Sci. Technol.* **2010**, *53*, 43–49.
(13) Song, Y.; Shen, Y.; Liu, H.; Lin, Y.; Li, M.; Nan, C. W. *J. Mater. Chem.* **2012**, *22*, 16491–16498.
(14) Xia, W.; Xu, Z.; Wen, F.; Zhang, Z. *Ceram. Int.* **2012**, *38*, 1071–1075.
(15) Chen, Q.; Chu, B. J.; Zhou, X.; Zhang, Q. M. *Appl. Phys. Lett.* **2007**, *91*, 062907.
(16) Xie, L.; Huang, X.; Wu, C.; Jiang, P. *J. Mater. Chem.* **2011**, *21*, 5897–5906.
(17) Chu, B. J.; Lin, M. R.; Neese, B.; Zhou, X.; Chen, Q.; Zhang, Q. M. *Appl. Phys. Lett.* **2007**, *91*, 122909.
(18) Dang, Z. M.; Wang, H. Y.; Peng, B.; Nan, C. W. *J. Electroceram.* **2008**, *21*, 381–384.
(19) Li, Y.; Huang, X.; Hu, Z.; Jiang, P.; Li, S.; Tanaka, T. *ACS Appl. Mater. Interfaces* **2011**, *3*, 4396–4403.
(20) Hammami, H.; Arous, M.; Lagache, M.; Kallel, A. *J. Alloys Compd.* **2007**, *430*, 1–8.
(21) Lunkenheimer, P.; Bobnar, V.; Pronin, A. V.; Ritus, A. I.; Volkov, A. A.; Loidl, A. *Phys. Rev. B* **2002**, *66*, 052105.
(22) Dang, Z. M.; Wang, H. Y.; Zhang, Y. H.; Qi, J. Q. *Macromol. Rapid Commun.* **2005**, *26*, 1185–1189.
(23) Zhou, T.; Zha, J. W.; Cui, R. Y.; Fan, B. H.; Yuan, J. K.; Dang, Z. M. *ACS Appl. Mater. Interfaces* **2011**, *3*, 2184–2188.
(24) Li, J.; Seok, S. I.; Chu, B.; Dogan, F.; Zhang, Q.; Wang, Q. *Adv. Mater.* **2009**, *21*, 217–221.
(25) Yu, K.; Wang, H.; Zhou, Y.; Bai, Y.; Niu, Y. *J. Appl. Phys.* **2013**, *113*, 034105.